



Optical Characterization of OMT-Coupled TES Bolometers for LiteBIRD

J. Hubmayr¹ · P. A. R. Ade² · A. Adler³ · E. Ally⁴ · D. Alonso⁵ · K. Arnold⁶, et al. [full author details at the end of the article]

Received: 1 November 2021 / Accepted: 24 July 2022 / Published online: 5 September 2022
This is a U.S. Government work and not under copyright protection in the US; foreign copyright protection may apply 2022

Abstract

Feedhorn- and orthomode transducer- (OMT) coupled transition edge sensor (TES) bolometers have been designed and micro-fabricated to meet the optical specifications of the LiteBIRD high frequency telescope (HFT) focal plane. We discuss the design and optical characterization of two LiteBIRD HFT detector types: dual-polarization, dual-frequency-band pixels with 195/280 GHz and 235/337 GHz band centers. Results show well-matched passbands between orthogonal polarization channels and frequency centers within 3% of the design values. The optical efficiency of each frequency channel is conservatively reported to be within the range 0.64–0.72, determined from the response to a cryogenic, temperature-controlled thermal source. These values are in good agreement with expectations and either exceed or are within 10% of the values used in the LiteBIRD sensitivity forecast. Lastly, we report a measurement of loss in Nb/SiN_x/Nb microstrip at 100 mK and over the frequency range 200–350 GHz, which is comparable to values previously reported in the literature.

Keywords CMB · TES · OMT · Low temperature detector · Bolometer

1 Introduction

LiteBIRD is a satellite-based low angular resolution cosmic microwave background (CMB) imager scheduled for launch in the late 2020s [1]. In the baseline configuration, LiteBIRD will image in 15 frequency bands by use of three telescopes [2, 3]. The low- and mid-frequency telescopes will use arrays of sinuous/lenslet-coupled transition edge sensor (TES) bolometers, and the development status of these arrays is described separately [4]. The high frequency telescope (HFT) on LiteBIRD—spanning the frequency range 195–402 GHz—will contain arrays of feedhorn/orthomode transducer (OMT)-coupled, polarization-sensitive TES bolometers. This detector architecture has been developed by NIST and collaborations over the previous decade, has been deployed in several ground-based CMB experiments [5–8], has been

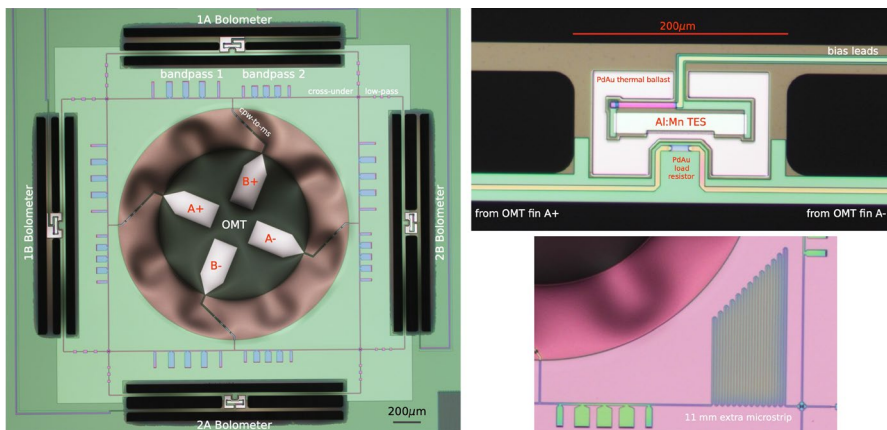


Fig. 1 *Left:* Optical micrograph of HF1 with labeled sub-components. A dark bolometer (not shown) is also included in each device. *Right top:* Zoom-in of TES bolometer with labeled sub-components. *Right bottom:* The HF2 design includes an additional length of Nb microstrip in one polarization channel to determine the superconducting transmission line loss at mm-wavelengths. (Color figure online)

produced for several near-term ground-based imagers to be deployed [9, 10], and is ready for use in the second balloon flight of SPIDER [11, 12]. An alternative OMT-coupled technology has been developed by NASA-Goddard [13] and is currently used in the CLASS experiment [14].

The application of OMT-coupled detectors to LiteBIRD is unique in several ways. Prior to this work, the highest frequency demonstration was at 280 GHz [12, 15], whereas the highest HFT band center frequency is 402 GHz. LiteBIRD's use of 100 mK cooling [16] in combination with MHz frequency division SQUID multiplexed (FDM) readout [17] explores a new regime within the TES superconducting transition temperature and sensor impedance (T_c - R_n) phase space, which impacts sensor dynamics. Additionally, it is widely known that in order to maximize the instantaneous sensitivity afforded by the space environment, the bolometers must have low thermal conductance and must be sufficiently insensitive to cosmic rays. We discussed space-optimized bolometers for LiteBIRD in a previous publication [18]. In this work, we characterize the key optical properties of two HFT detector types: dual-polarization, dual-band feedhorn/OMT-coupled pixels with design band centers of 195/280 GHz and 235/337 GHz. We refer to these pixel types as ‘HF1’ and ‘HF2,’ respectively. ‘HF3’ is a 402 GHz monochromatic pixel, which is not further discussed here.

2 Device Description and Fabrication

A wafer containing both HF1 and HF2 pixels was fabricated in the NIST Boulder Microfabrication Facility. Figure 1 shows an optical micrograph of an HF1 pixel with labeled sub-components used for polarization separation, transmission line impedance transformation, frequency band diplexing, and relative power sensing

over a 2:1 bandwidth ratio. Each chip contains five TES bolometers: two for each polarization in each frequency band and one dark detector (not connected to the OMT circuit) used for the dark power subtraction technique described in Sect. 3.2. These devices are frequency scaled versions of the multichroic polarimeters described in McMahon et al. [19]. However, in this implementation, we replace the mode-cleaning 180° hybrids with symmetrically fed lumped-element termination resistors located on each bolometer island, annotated as ‘PdAu load resistor’ in Fig. 1. This termination approach has been used in other CMB detectors [20]. And its implementation decreases the size of the TES bolometer island by a factor of 5 relative to the Advanced ACTPol bolometers [21], which in turn decreases both the bolometer time constant (enabling the use of LiteBIRD’s rapid half-wave plate polarization modulator [22]) and the cross section to cosmic rays.

Fabrication largely follows the description in Duff et al. [21] but with modifications specific to LiteBIRD. We reduce the thermal SiN_x thickness to 1 μm , necessary for space-optimized low thermal conductance bolometers. MHz frequency division multiplexing requires a normal TES resistance $R_n \sim 1 \Omega$. As such we utilize a $120 \times 20 \times 0.18\mu\text{m}^3$ 2200 ppma Al/Mn sensor. The superconducting transition temperature (T_c) of Al/Mn films can be tuned both by Mn concentration and heat treatment [23]. In this work, we bake the film at 230°C for 10 min, resulting in $T_c = 208 \text{ mK}$ and $R_n = 0.9 \Omega$. Lastly, the aforementioned termination resistor consists of a 50 nm thick sputter-deposited PdAu film patterned to $15.675 \times 5\mu\text{m}^2$. These dimensions yield a resistance of $2Z_{\text{ms}} = 22\Omega$, where Z_{ms} is the impedance of the superconducting microstrip carrying the mm-wave signal. The Nb/ SiN_x /Nb microstrip transmission line geometry used to connect the sub-components remains unchanged: 200 nm thick Nb ground plane; 350 nm thick SiN_x dielectric; and a 400 nm thick 5 μm wide straight-wall etched Nb top conductor.

As shown in the lower right of Fig. 1, we add 11 mm of additional microstrip transmission line in the ‘B’ polarization arm of both frequency bands within the HF2 pixel. This feature enables a measurement of mm-wave loss within the superconducting transmission line as described in Sect. 3.3.

3 Experimental Results

Devices were packaged into Au-plated split-block waveguide modules machined from brass, which place the planar OMTs within circular waveguides at roughly one-quarter wave away from reflective backshorts. The waveguide cutoff frequency is designed to be approximately 10% lower than the lowest passband frequency of the diplexer and has negligible impact on the passband shape. Conical feedhorns mount to the sky side of the brass modules for optical coupling to the thermal sources used in this work. Four brass modules, two for each frequency type, were mounted on a mK assembly board, which contained elements for TES bias and SQUID readout.

Due to the availability of room temperature electronics at NIST, we read out the sensors by use of a time division SQUID multiplexer (TDM) [24], despite engineering the sensors for MHz FDM. The standard DC-bias TES circuit [25] is used in a one column by 24 row configuration. A custom interface chip with 66.2 $\text{m}\Omega$ shunt

resistors and 65 μH Nyquist inductors was fabricated and mounted to the mK assembly board, which enables the readout of $\sim 1 \Omega$ sensors with our TDM electronics.

The assembly board was mounted to the 100-mK stage of a 2-stage ADR cryostat testbed. We configured the dewar in two separate ways. For passband measurements, a 150 mm zotefoam window, filter stacks at 70 K and 4 K, and a 420-GHz low-pass quasi-optical filter allowed coupling the detectors to a Martin-Puplet-type Fourier transform spectrometer (FTS), which has 0.8 GHz resolution. When measuring optical efficiency, we installed a beam-filling cryogenic temperature controlled blackbody mounted to the 4K stage and placed the 420-GHz low-pass filter between the blackbody source and the mK assembly board. The pixels were exchanged in the two configurations. For efficiency measurements, we used bolometers with thermally isolating legs (see Fig. 1 *upper right*) to achieve high sensitivity. For passband measurements that require higher dynamic range, we used continuous membrane bolometers (no leg definition) to achieve high thermal conductance.

3.1 Passbands

Figure 2 shows the measured passbands of an HF1 and HF2 device. We subtract a linear drift from the raw single-sided interferograms and follow the symmetrization-convolution method [26] to produce the phase corrected spectra shown. A model to account for the spectral response of components between the FTS and the horn/detector system has not been applied here, and therefore, the data include the effects of our cryogenic filter stack and the FTS spectral response itself. We find that the passbands from orthogonal polarizations are well matched in all four bands. The fractional difference in center frequency within a polarization pair is at most 0.7%. Limited by the measurement signal-to-noise ratio, the out-of-band response is constrained to $\lesssim 1\%$ of the peak transmission value.

The dashed-black curve in Fig. 2 is the simulated diplexer response based on 2.5D electro-magnetic simulations. We simulate each 5-pole stub filter individually and then use the responses in a circuit model that connects the two stub filters together with optimized electrical lengths of lossless transmission line. The model assumes that the SiN_x relative dielectric constant (ϵ_r) is 6.8 and the Nb London penetration depth is 85 nm.

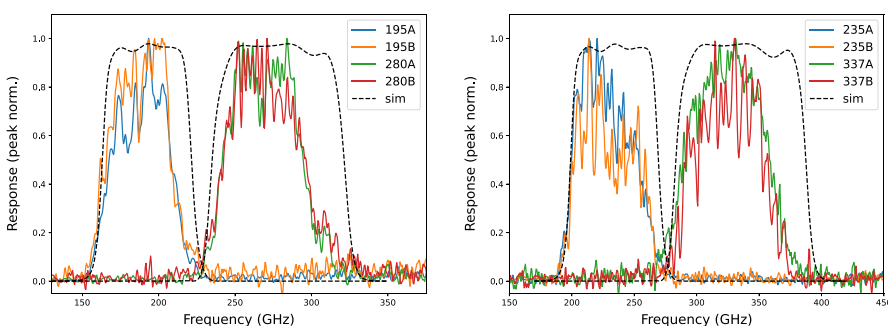


Fig. 2 Passband measurements of HF1 (*Left*) and HF2 (*Right*). (Color figure online)

The measured center frequencies are within 3% of the design value. We find good agreement with the model on the lower edge of each band; however, this is not true for the upper edge. The measured bandwidths are $\sim 10\%$ and $\sim 20\%$ less than the designed bandwidths in the lower and upper band in each pixel type.

3.2 Optical Efficiency

To measure the device optical efficiency, the blackbody source was swept from 5K to 13K and the electrical power dissipated in each sensor determined from bolometer IV curves acquired at each cold load temperature, T . Since we do not measure the bolometer power plateaus in the no loading condition (which would require a separate experimental configuration and cooldown), we do not determine the absolute power absorbed in the bolometers. Rather because the TES bolometer is a relative power meter, we track the change in sensor electrical power (P) versus the change in blackbody temperature from 5 K, its lowest temperature. The optical efficiency is defined as

$$\eta = \frac{\Delta P}{\Delta P_{\text{load}}} = \frac{P(5\text{K}) - P(T)}{P_{\text{load}}(T) - P_{\text{load}}(5\text{K})}, \quad (1)$$

where P_{load} is the calculated power in a single electromagnetic mode from an ideal blackbody source:

$$P_{\text{load}} = \int \frac{h\nu}{e^{\frac{h\nu}{kT}} - 1} F(\nu) d\nu. \quad (2)$$

In this equation, h is the Planck constant, ν is frequency, k is the Boltzmann constant, T is the blackbody temperature, and $F(\nu)$ is the measured, normalized passband using the condition [27]

$$\frac{\int F^2(\nu) d\nu}{\int F(\nu) d\nu} = 1. \quad (3)$$

The electrical power determined from IV curves is evaluated at constant normal resistance (R_n) fraction in the range $0.5 < R/R_n < 0.7$. As ΔP typically differs by $<2\%$ over this range, the exact resistance cut has little impact on the final result. The left side of Fig. 3 shows an example ΔP versus ΔT_{load} data set, including the response of both 337-GHz polarization bolometer channels, the dark bolometer, and the calculated ΔP_{load} (labeled $\eta = 1$). As has been previously observed [15], we find a small response in the dark bolometer channel to the changing cold load temperature. When calculating η , we subtract this device-specific ‘dark power’ from each optical channel ΔP . To isolate the efficiency of the horn-to-bolometer detector system, we also remove the expected loss in the 420-GHz low-pass filter. This loss (< 0.09 for all bands) is estimated from the band-averaged room temperature transmission spectra of the filter. We find $\eta = 0.64, 0.68, 0.65$, and 0.72 for the 195, 235, 280, and 337-GHz frequency channels, respectively. If we define η relative to the designed passband, the values are 8–25% lower due to the reduced bandwidth discussed in Sect. 3.1.

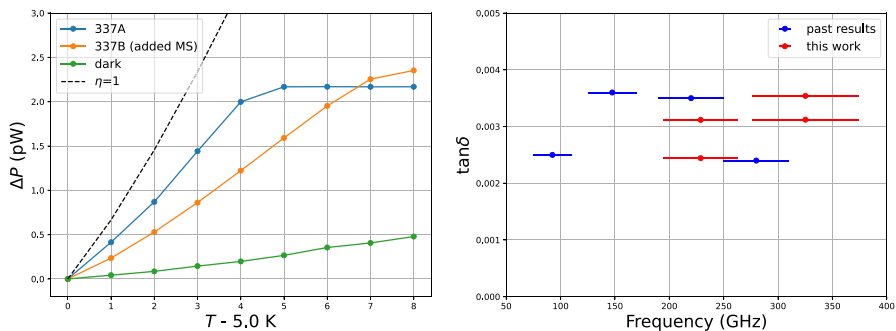


Fig. 3 *Left:* Change in TES electrical power versus change in blackbody temperature from 5K for the 337-GHz band. The 337A channel saturates above $T = 9\text{K}$. The lower response in 337B is due to loss within the additional microstrip transmission line. The nonzero response of the dark bolometer is subtracted from the optical ΔP when determining the optical efficiency. *Right:* SiN_x dielectric loss tangent extracted from differential line-length loss measurements. The horizontal bars denote the edges of the passband in the measurement. Here, ‘past results’ are previously unreported measurements extending to lower frequencies. (Color figure online)

3.3 Millimeter-Wave Loss in Superconducting Transmission Line

The use of low-loss transmission lines is critical to the performance of many millimeter-wave detectors. Since the ‘B’ polarization arm of HF2 includes an added length of transmission line, the ratio η_B/η_A (where the subscript refers to the polarization channel) is a direct measurement of loss in the $\text{Nb}/\text{SiN}_x/\text{Nb}$ microstrip. We find that the loss in a band centered on 229 GHz (325 GHz) is 3.8%/mm (5.4%/mm).

If the loss is entirely due to the dielectric, the loss tangent may be calculated as

$$\tan \delta = \frac{c}{2\pi x \sqrt{\epsilon_r} f_c} \ln \eta_A/\eta_B, \quad (4)$$

where c is the speed of light in vacuum, the differential line length $x = 11\text{ mm}$, $\epsilon_r = 6.8$, and f_c is the measured center frequency. The results show $\tan \delta \sim 3 \times 10^{-3}$, which is consistent with our previous measurements (see Fig. 3 right), and is comparable to other direct measurements of mm-wave loss in SiN_x [28–30] and SiO_x [31, 32]. Recently, the use of amorphous silicon [33] and hydrogenated amorphous silicon carbide [34] dielectrics has resulted in an order of magnitude lower loss at mm-wavelengths.

4 Discussion and Conclusions

The measured optical efficiency in all four bands compares well with the $\eta = 0.7$ top-hat passband assumption used in the LiteBIRD sensitivity forecasting [35]. Based on a model that uses the simulated transmission of all on-chip sub-components and assumes $\tan \delta = 3 \times 10^{-3}$, we expect $\eta = 0.77, 0.76, 0.69, 0.68$ for the 195,

235, 280, and 337-GHz frequency channels, respectively. Measurement within 17% of expectations for all four frequency bands is reasonable given uncertainties in both the measurement and prediction.

A main contributor to the uncertainty of η stems from the dark bolometer response treatment. The source may be thermal or optical. We have evidence to suggest the latter. The technique implicitly assumes that the electrical power change of the dark bolometer within a detector package is equal to the power that bypasses the OMT circuitry and is directly absorbed in each optically coupled bolometer. The observed level of dark power coupling is reasonable based on 3D electromagnetic simulations of power leakage into the 100- μm OMT-probe waveguide gap. But given the cavity-like geometry of the detector package, positional dependence is expected, and therefore, the dark bolometer response may not be representative. Knowledge of in- versus out-of-band pickup is also lacking and is required to properly extract η in the presence of parasitic optical response. Given these considerations, the dark power subtraction technique may lead to a maximum 13% negative bias on η , but will not lead to a positive bias.

Note that, the 10% dark bolometer response seen in Fig. 3 is unique to the single-pixel detector packaging used in this prototyping phase. The level of stray-light coupling is a strong function of the waveguide gap size, which is limited here by standard machining techniques. The gap size will be reduced by more than a factor of six in the flight arrays by use of precision silicon micro-machined coupling wafers, and from this, we anticipate a substantial reduction in the dark response relative to what is presented here.

Passband bandwidths lower than expectations have not been observed in similar diplexer designs [15], yet a compelling explanation remains outstanding and is the subject of ongoing work. Possible explanations may include decreased OMT bandwidth resulting from an out-of-tolerance waveguide diameter in the detector/feedhorn package, over-etching the diplexer main transmission line, or dispersion from anomalous Nb properties.

In summary, we have designed and fabricated feedhorn/OMT-coupled devices as part of the development of the LiteBIRD HFT focal plane. We characterize key optical properties for four out of the five LiteBIRD HFT frequency channels and find passbands comparable to the design with no observable out-of-band response, optical efficiency in agreement with expectations, and $\tan \delta \simeq 3 \times 10^{-3}$ at 100 mK over the frequency range 200–350 GHz in Nb/SiN_x/Nb microstrip. These results represent an important step in technical maturity for LiteBIRD and are the highest frequency demonstration of OMT-coupled TES bolometers to date.

Acknowledgements This work is supported by NASA under grant no. 80NSSC18K0132.

References

1. M. Hazumi, P. Ade, A. Adler et al., SPIE **11443**, 431–450 (2020)
2. Y. Sekimoto, P.A.R. Ade, A. Adler et al., SPIE **11453**, 189–209 (2020)
3. L. Montier, B. Mot, P. de Bernardis et al., SPIE **11443**, 451–471 (2020)
4. B. Westbrook, C. Raum, S. Beckman et al., SPIE **11443**, 114435Q (2020)

5. J. E. Austermann, K. A. Aird, J. A. Beall, et al. SPIE 8452 (2012). 1210,4970
6. R. Thornton, P. Ade, S. Aiola et al., *Astrophys. J. Sup.* **227**(2), 21 (2016)
7. S. Henderson, R. Allison, J. Austermann et al., *J. Low Temp. Phys.* **184**(3), 772–779 (2016)
8. S. Dicker, P. Ade, J. Aguirre et al., *J. Low Temp. Phys.* **176**(5), 808–814 (2014)
9. P. Ade, J. Aguirre, Z. Ahmed et al., *J. Cos. Astro. Phys.* **02**, 056 (2019)
10. H. Li, S.-Y. Li, Y. Liu et al., *Natl. Sci. Rev.* **6**(1), 145–154 (2019)
11. J. Hubmayr, J.E. Austermann, J.A. Beall et al., SPIE **9914**, 99140V (2016)
12. A. Bergman, P. Ade, S. Akers et al., *J. Low Temp. Phys.* **5**, 1075–1084 (2018)
13. K. Rostem, C. Bennett, D. Chuss et al., SPIE **8452**, 84521N (2012)
14. T. Essinger-Hileman, A. Ali, M. Amiri et al., SPIE **9153**, 91531I (2014)
15. S. Walker, C.E. Sierra, J.E. Austermann et al., *J. Low Temp. Phys.* **199**(3), 891–897 (2020)
16. J.-M. Duval, T. Prouvé, P. Shirron, et al. *J. Low Temp. Phys.* **199** (2020)
17. T. Lanting, H.-M. Cho, J. Clarke et al., *Appl. Phys. Lett.* **86**(11), 112511 (2005)
18. G. Jaehnig, K. Arnold, J. Austermann, et al. *J. Low Temp. Phys.* **199** (2020)
19. J. McMahon, J. Beall, D. Becker et al., *J. Low Temp. Phys.* **167**(5–6), 879–884 (2012)
20. M. Myers et al., *Appl. Phys. Lett.* **86**, 114103 (2005)
21. S.M. Duff, J. Austermann, J. Beall et al., *J. Low Temp. Phys.* **184**(3), 634–641 (2016)
22. Y. Sakurai, T. Matsumura, N. Katayama et al., SPIE **11453**, 114534E (2020)
23. D. Li, J. Austermann, Beall, et al., *J. Low Temp. Phys.* **184**(1), 66–73 (2016)
24. P.A.J. de Korte, J. Beyer, S. Deiker et al., *Rev. Sci. Inst.* **74**, 3807–3815 (2003)
25. K. D. Irwin and G. C. Hilton. In *Cryogenic Particle Detection*. Springer (2005), pp. 63–150
26. M.L. Forman, W.H. Steel, G.A. Vanasse, *JOSA* **56**(1), 59–63 (1966)
27. BICEP2 Collaboration, P. A. R. Ade, R. W. Aikin, et al. *Astrophys. J.* **792**, 1 (2014):62. 1403.4302
28. G. Cataldo, J.A. Beall, H.-M. Cho et al., *Opt. Lett.* **37**(20), 4200–4202 (2012)
29. A. Endo, C. Sfiligoj, S.J.C. Yates et al., *Appl. Phys. Lett.* **103**(3), 032601 (2013). <https://doi.org/10.1063/1.4813816>
30. S. Hailey-Dunsheath, P. Barry, C. Bradford et al., *J. Low Temp. Phys.* **176**(5), 841–847 (2014)
31. J. Gao, A. Vayonakis, O. Noroozian, et al. In *AIP Conference Proceedings*, volume 1185. American Institute of Physics (2009), pp. 164–167
32. C.L. Chang, P.A.R. Ade, Z. Ahmed et al., *IEEE Trans. Appl. Sup.* **25**(3), 1–5 (2015)
33. S. Hähnle, K. Kouwenhoven, B. Buijtendorp et al., *Phys. Rev. Appl.* **16**, 014019 (2021)
34. B. Buijtendorp, S. Vollebregt, K. Karatsu, et al. arXiv preprint [arXiv:2110.03500](https://arxiv.org/abs/2110.03500) (2021)
35. T. Hasebe. *J. Low Temp. Phys. This Special Issue* (2021)

Publisher's Note Springer Nature remains neutral with regard to jurisdictional claims in published maps and institutional affiliations.

Springer Nature or its licensor holds exclusive rights to this article under a publishing agreement with the author(s) or other rightsholder(s); author self-archiving of the accepted manuscript version of this article is solely governed by the terms of such publishing agreement and applicable law.

Authors and Affiliations

- J. Hubmayr¹  · P. A. R. Ade² · A. Adler³ · E. Ally⁴ · D. Alonso⁵ · K. Arnold⁶ ·
D. Auguste⁷ · J. Aumont⁸ · R. Aurlien⁹ · J. E. Austermann¹ · S. Azzoni^{5,10} ·
C. Baccigalupi^{11,12,13} · A. J. Banday⁸ · R. Banerji⁹ · R. B. Barreiro¹⁴ ·
N. Bartolo^{15,16} · S. Basak¹⁷ · E. Battistelli^{18,19} · L. Bautista⁸ · J. A. Beall¹ · D. Beck²⁰ ·
S. Beckman²¹ · K. Benabed²² · J. Bermejo-Ballesteros²³ · M. Bersanelli^{24,25} ·
J. Bonis⁷ · J. Borriil²⁶ · F. Bouchet²² · F. Boulanger⁴ · S. Bounissou²⁷ ·
M. Brilenkov⁹ · M. L. Brown²⁸ · M. Bucher²⁹ · E. Calabrese² · M. Calvo³⁰ ·
P. Campeti³¹ · A. Carones^{32,33} · F. J. Casas¹⁴ · A. Catalano³⁴ · A. Challinor^{35,36,37} ·
V. Chan³⁸ · K. Cheung^{21,26,39} · Y. Chinone^{10,40} · C. Chiocchetta⁴¹ · S. E. Clark^{20,42} ·
L. Clermont⁴³ · S. Clesse⁴⁴ · J. Cliche⁴⁵ · F. Columbro^{18,19} · J. A. Connors¹ ·

- A. Coppolecchia^{18,19} · W. Coulton¹⁰ · J. Cubas²³ · A. Cukierman^{20,21} · D. Curtis³⁹ · F. Cuttaia⁴⁶ · G. D'Alessandro^{18,19} · K. Dachlythra³ · P. de Bernardis^{18,19} · T. de Haan⁴⁷ · E. de la Hoz^{14,48} · M. De Petris^{18,19} · S. Della Torre⁴⁹ · J. J. Daz Garca⁵⁰ · C. Dickinson²⁸ · P. Diego-Palazuelos^{14,48} · M. Dobbs⁴⁵ · T. Dotani^{51,52} · D. Douillet⁷ · E. Doumayrou⁵³ · L. Duband⁵⁴ · A. Ducout¹⁰ · S. M. Duff¹ · J. M. Duval⁵⁴ · K. Ebisawa⁵¹ · T. Ellefrot²⁶ · H. K. Eriksen⁹ · J. Errard²⁹ · T. Essinger-Hileman⁵⁵ · S. Farrens⁵³ · F. Finelli^{46,56} · R. Flauger⁶ · K. Fleury-Frenette⁴³ · C. Franceschet^{24,25} · U. Fuskeland⁹ · L. Galli⁵⁷ · S. Galli²² · M. Galloway⁹ · K. Ganga²⁹ · J. R. Gao⁵⁸ · R. T. Genova-Santos^{50,59} · M. Georges⁴³ · M. Gerbino⁶⁰ · M. Gervasi^{49,61} · T. Ghigna^{5,10} · S. Giardiello⁴¹ · E. Gjerlw⁹ · R. Gonzlez Gonzles⁵⁰ · M. L. Gradziel⁶² · J. Grain²⁷ · L. Grandsire²⁹ · F. Grupp⁶³ · A. Gruppuso^{46,56} · J. E. Gudmundsson³ · N. W. Halverson⁶⁴ · J. Hamilton²⁹ · P. Hargrave² · T. Hasebe¹⁰ · M. Hasegawa⁴⁷ · M. Hattori⁶⁵ · M. Hazumi^{10,47,51,52} · S. Henrot-Versill⁷ · B. Hensley⁶⁶ · D. Herman⁹ · D. Herranz¹⁴ · G. C. Hilton¹ · E. Hivon²² · R. A. Hlozek³⁸ · D. Hoang⁶⁷ · A. L. Hornsby²¹ · Y. Hoshino⁶⁸ · K. Ichiki⁶⁹ · T. Iida⁷⁰ · T. Ikemoto⁴⁷ · H. Imada⁷¹ · K. Ishimura⁷² · H. Ishino⁷³ · G. Jaehnig⁶⁴ · M. Jones⁵ · T. Kaga⁷⁴ · S. Kashima⁷¹ · N. Katayama¹⁰ · A. Kato⁴⁷ · T. Kawasaki⁷⁵ · R. Keskitalo^{21,26,39} · C. Kintziger⁴³ · T. Kisner²⁶ · Y. Kobayashi^{76,77} · N. Kogiso⁷⁸ · A. Kogut⁵⁵ · K. Kohri⁴⁷ · E. Komatsu³¹ · K. Komatsu⁷³ · K. Konishi⁷⁹ · N. Krachmalnicoff^{11,12,13} · I. Kreykenbohm⁸⁰ · C. L. Kuo^{20,81} · A. Kushino⁸² · L. Lamagna^{18,19} · J. V. Lanen¹ · G. Laquaniello⁷ · M. Lattanzi⁶⁰ · A. T. Lee^{21,83} · C. Leloup²⁹ · F. Levrier⁴ · E. Linder^{39,83} · M. J. Link¹ · A. I. Lonappan¹¹ · T. Louis⁷ · G. Luzzi⁸⁴ · J. Macias-Perez³⁴ · T. Maciaszek⁸⁵ · B. Maffei²⁷ · D. Maino²⁴ · M. Maki⁴⁷ · S. Mandelli^{24,25} · M. Maris⁸⁶ · B. Marquet⁴³ · E. Martnez-Gonzlez¹⁴ · F. A. Martire¹⁴ · S. Masi^{18,19} · M. Massa⁵⁷ · M. Masuzawa⁴⁷ · S. Matarrese^{15,16,87,88} · F. T. Matsuda⁵¹ · T. Matsumura¹⁰ · L. Mele^{18,19} · A. Mennella^{24,25} · M. Migliaccio^{32,33} · Y. Minami⁸⁹ · K. Mitsuda⁷¹ · A. Moggi⁵⁷ · M. Monelli³¹ · A. Monfardini³⁰ · J. Montgomery⁴⁵ · L. Montier⁸ · G. Morgante⁴⁶ · B. Mot⁸ · Y. Murata⁵¹ · J. A. Murphy⁶² · M. Nagai⁷¹ · Y. Nagano⁷³ · T. Nagasaki⁴⁷ · R. Nagata⁵¹ · S. Nakamura⁹⁰ · R. Nakano^{51,77} · T. Namikawa^{35,37} · F. Nati^{49,61} · P. Natoli^{41,60} · S. Nerval³⁸ · N. Neto Godry Farias⁸³ · T. Nishibori⁷⁴ · H. Nishino⁴⁷ · F. Noviello² · G. C. O'Neil¹ · C. O'Sullivan⁶² · K. Odagiri⁵¹ · H. Ochi⁹⁰ · H. Ogawa⁷⁸ · H. Ogawa⁵¹ · S. Oguri⁵¹ · H. Ohsaki⁷⁶ · I. S. Ohta⁹¹ · N. Okada⁷⁸ · L. Pagano^{27,41,60} · A. Paiella^{18,19} · D. Paoletti^{46,56} · G. Pascual Cisneros¹⁴ · A. Passerini^{49,61} · G. Patanchon²⁹ · V. Pelgrim⁹² · J. Peloton⁷ · V. Pettorino⁵³ · F. Piacentini^{18,19} · M. Piat²⁹ · G. Piccirilli³² · F. Pinsard⁵³ · G. Pisano¹⁸ · J. Plesseria⁴³ · G. Polenta⁸⁴ · D. Poletti^{49,61} · T. Prouv⁵⁴ · G. Puglisi³⁹ · D. Rambaud⁸ · C. Raum²¹ · S. Realini²⁴ · M. Reinecke³¹ · C. D. Reintsema¹ · M. Remazeilles²⁸ · A. Ritacco^{4,27} · P. Rosier⁷ · G. Roudil⁸ · J. Rubino-Martin^{50,59} · M. Russell¹⁶ · H. Sakurai⁷⁶ · Y. Sakurai^{10,73} · M. Sandri⁴⁶ · M. Sasaki⁸⁰ · G. Savini⁹³ · D. Scott⁹⁴ · J. Seibert⁶ · Y. Sekimoto^{47,51,77} · B. Sherwin^{35,37,83} · K. Shinozaki⁷⁴ · M. Shiraishi⁹⁵ · P. Shirron⁵⁵ · A. Shitsov⁹³ · G. Signorelli⁵⁷ · G. Smecher^{45,96} · F. Spinella⁵⁷ · J. Starck⁵³ · S. Stever^{10,73} · R. Stompor^{29,97} · R. Sudiwala² · S. Sugiyama⁶⁸ · R. Sullivan⁹⁴ · A. Suzuki²⁶ · J. Suzuki⁴⁷ · T. Suzuki⁵¹ · T. L. Svalheim⁹ · E. Switzer⁵⁵ · R. Takaku^{51,98} · H. Takakura^{51,77} · S. Takakura¹⁰ · Y. Takase⁷³ · Y. Takeda⁷⁴ · A. Tartari^{57,99} · D. Tavagnacco⁴⁶ · A. Taylor⁵ · E. Taylor²¹ · Y. Terao⁷⁶ · L. Terenzi⁴⁶ · J. Therneau²⁹

H. Thommesen⁹ · K. L. Thompson^{20,81} · B. Thorne⁵ · T. Toda⁷³ · M. Tomasi^{24,25} ·
M. Tominaga^{51,98} · N. Trappe⁶² · M. Tristram⁷ · M. Tsuji⁹⁵ · M. Tsujimoto⁵¹ ·
C. Tucker² · R. Ueki⁴⁷ · J. N. Ullom¹ · K. Umemori⁴⁷ · L. Vacher⁸ · J. Van Lanen¹ ·
G. Vermeulen³⁰ · P. Vielva¹⁴ · F. Villa⁴⁶ · M. R. Vissers¹ · N. Vittorio^{32,33} ·
B. Wandelt²² · W. Wang²⁹ · I. K. Wehus⁹ · J. Weller⁶³ · B. Westbrook²¹ ·
G. Weymann-Despres⁷ · J. Wilms⁸⁰ · B. Winter^{93,100} · E. J. Wollack⁵⁵ ·
N. Y. Yamasaki⁵¹ · T. Yoshida⁵¹ · J. Yumoto⁷⁶ · K. Watanuki⁵¹ · A. Zacchei⁸⁶ ·
M. Zannoni^{49,61} · A. Zonca¹⁰¹

✉ J. Hubmayr
hubmayr@nist.gov

¹ National Institute of Standards and Technology, Quantum Sensors Group, Boulder, CO 80305, USA

² School of Physics and Astronomy, Cardiff University, Cardiff CF10 3XQ, UK

³ The Oskar Klein Centre, Department of Physics, Stockholm University, 106 91 Stockholm, Sweden

⁴ Laboratoire de Physique de l'École Normale Supérieure, ENS, Université PSL, CNRS, Sorbonne Université, Université de Paris, 75005 Paris, France

⁵ Department of Physics, University of Oxford, Denys Wilkinson Building, Keble Road, Oxford OX1 3RH, United Kingdom

⁶ Department of Physics, University of California, San Diego, San Diego, CA 92093-0424, USA

⁷ Université Paris-Saclay, CNRS/IN2P3, IJCLab, 91405 Orsay, France

⁸ IRAP, Université de Toulouse, CNRS, CNES, UPS, Toulouse, France

⁹ Institute of Theoretical Astrophysics, University of Oslo, Blindern, Oslo, Norway

¹⁰ Kavli Institute for the Physics and Mathematics of the Universe (Kavli IPMU, WPI), UTIAS, The University of Tokyo, Kashiwa, Chiba 277-8583, Japan

¹¹ International School for Advanced Studies (SISSA), Via Bonomea 265, 34136 Trieste, Italy

¹² INFN Sezione di Trieste, via Valerio 2, 34127 Trieste, Italy

¹³ IFPU, Via Beirut, 2, 34151 Trieste, Grignano, Italy

¹⁴ Instituto de Fisica de Cantabria (IFCA, CSIC-UC), Avenida los Castros SN, 39005 Santander, Spain

¹⁵ Dipartimento di Fisica e Astronomia “G. Galilei”, Universita’ degli Studi di Padova, via Marzolo 8, 35131 Padova, Italy

¹⁶ INFN Sezione di Padova, via Marzolo 8, 35131 Padova, Italy

¹⁷ School of Physics, Indian Institute of Science Education and Research Thiruvananthapuram, Maruthamala PO, Vithura, Thiruvananthapuram, Kerala 695551, India

¹⁸ Dipartimento di Fisica, Università La Sapienza, P. le A. Moro 2, Roma, Italy

¹⁹ INFN Sezione di Roma, P.le A. Moro 2, 00185 Roma, Italy

²⁰ Department of Physics, Stanford University, Standford, CA 94305-4060, USA

²¹ Department of Physics, University of California, Berkeley, Berkeley, CA 94720, USA

²² Institut d’Astrophysique de Paris, CNRS/Sorbonne Université, Paris, France

²³ Instituto Universitario Ignacio Da Riva (IDR/UPM), Universidad Politécnica de Madrid, Plaza Cardenal Cisneros, 3, 28040 Madrid, Spain

- ²⁴ Dipartimento di Fisica, Universita' degli Studi di Milano, Via Celoria 16 - 20133, Milano, Italy
- ²⁵ INFN Sezione di Milano, Via Celoria 16 - 20133, Milano, Italy
- ²⁶ Lawrence Berkeley National Laboratory (LBNL), Computational Cosmology Center, Berkeley, CA 94720, USA
- ²⁷ Universit Paris-Saclay, CNRS, Institut d'Astrophysique Spatiale, 91405 Orsay, France
- ²⁸ University of Manchester, Manchester M13 9PL, United Kingdom
- ²⁹ AstroParticle and Cosmology (APC) - University Paris Diderot, CNRS/IN2P3, CEA/Irfu, Obs de Paris, Sorbonne Paris Cité, France
- ³⁰ Université Grenoble Alpes, CNRS, Grenoble INP, Institut Nel, 38000 Grenoble, France
- ³¹ Max-Planck-Institute for Astrophysics, Garching, Germany
- ³² Dipartimento di Fisica, Università di Roma Tor Vergata, Via della Ricerca Scientifica, 1, 00133 Roma, Italy
- ³³ INFN Sezione di Roma2, Università di Roma Tor Vergata, via della Ricerca Scientifica 1, 00133 Roma, Italy
- ³⁴ Université Grenoble Alpes, CNRS, LPSC-IN2P3, 53, avenue des Martyrs, 38000 Grenoble, France
- ³⁵ DAMTP, Centre for Mathematical Sciences, Wilberforce Road, Cambridge CB3 0WA, UK
- ³⁶ Institute of Astronomy, Madingley Road, Cambridge CB3 0HA, UK
- ³⁷ Kavli Institute for Cosmology Cambridge, Madingley Road, Cambridge CB3 0HA, UK
- ³⁸ David A. Dunlap Department of Astronomy and Astrophysics, 50 St. George Street, Toronto, ON M5S3H4, USA
- ³⁹ University of California, Berkeley, Space Science Laboratory, Berkeley, CA 94720, USA
- ⁴⁰ School of Science, Research Center for the Early Universe, RESCEU, University of Tokyo, Tokyo, Japan
- ⁴¹ Dipartimento di Fisica e Scienze della Terra, Università di Ferrara, Via Saragat 1, 44122 Ferrara, Italy
- ⁴² Kavli Institute for Particle Astrophysics & Cosmology (KIPAC), Stanford University, Stanford, CA 94305, USA
- ⁴³ Centre Spatial de Lige, Lige, Belgium
- ⁴⁴ Universit Libre de Bruxelles, Bruxelles, Belgium
- ⁴⁵ Physics Department, McGill University, Montreal, QC H3A 0G4, Canada
- ⁴⁶ INAF - OAS Bologna, via Piero Gobetti 93/3 40129 Bologna, Italy
- ⁴⁷ High Energy Accelerator Research Organization (KEK), Tsukuba, Ibaraki 305-0801, Japan
- ⁴⁸ Dpto. de Fsica Moderna, Universidad de Cantabria, Avda. los Castros s/n, 39005 Santander, Spain
- ⁴⁹ INFN Sezione Milano Bicocca, Piazza della Scienza 3, 20126 Milano, Italy
- ⁵⁰ Instituto de Astrofsica de Canarias, 38200 La Laguna, Tenerife, Canary Islands, Spain
- ⁵¹ Japan Aerospace Exploration Agency (JAXA), Institute of Space and Astronautical Science (ISAS), Sagamihara, Kanagawa 252-5210, Japan
- ⁵² The Graduate University for Advanced Studies (SOKENDAI), Miura District, Kanagawa 240-0115, Hayama, Japan
- ⁵³ AIM, CEA, CNRS, Universit Paris-Saclay, Universit de Paris, 91191 Gif-sur-Yvette, France

- ⁵⁴ Université Grenoble Alpes, CEA, IRIG-DSBT, 38000 Grenoble, France
⁵⁵ NASA Goddard Space Flight Center, Greenbelt, USA
⁵⁶ INFN Sezione di Bologna, Viale C. Berti Pichat 6/2, 40127 Bologna, Italy
⁵⁷ INFN Sezione di Pisa, Largo Bruno Pontecorvo 3, 56127 Pisa, Italy
⁵⁸ SRON Netherlands Institute for Space Research, Sorbonnelaan 2, 3584 CA Utrecht, The Netherlands
⁵⁹ Departamento de Astrofsica, Universidad de La Laguna (ULL), 38206 La Laguna, Tenerife, Spain
⁶⁰ INFN Sezione di Ferrara, Via Saragat 1, 44122 Ferrara, Italy
⁶¹ Physics Department, University of Milano Bicocca, p.zza della Scienza 3, 20126 Milan, Italy
⁶² National University of Ireland Maynooth, Co. Kildare, Ireland
⁶³ USM, The Ludwig Maximilians University of Munich, Munich, Germany
⁶⁴ Center for Astrophysics and Space Astronomy, University of Colorado, Boulder, CO 80309, USA
⁶⁵ Graduate School of Science, Astronomical Institute, Tohoku University, Sendai 980-8578, Japan
⁶⁶ Department of Astrophysical Sciences, Princeton University, Peyton Hall, Princeton, NJ 08544, USA
⁶⁷ University of Science and Technology of Hanoi, Hanoi, Vietnam
⁶⁸ Saitama University, Saitama 338-8570, Japan
⁶⁹ Nagoya University, Kobayashi-Masukawa Institute for the Origin of Particle and the Universe, Aichi 464-8602, Japan
⁷⁰ ispace,inc., Tokyo, Japan
⁷¹ National Astronomical Observatory of Japan, Mitaka, Tokyo 181-8588, Japan
⁷² Waseda University, Tokyo, Japan
⁷³ Department of Physics, Okayama University, Okayama 700-8530, Japan
⁷⁴ Japan Aerospace Exploration Agency (JAXA), Research and Development Directorate, Tsukuba, Ibaraki 305-8505, Japan
⁷⁵ Kitasato University, Sagamihara, Kanagawa 252-0373, Japan
⁷⁶ The Institute for Solid State Physics (ISSP), The University of Tokyo, Kashiwa, Chiba 277-8581, Japan
⁷⁷ The University of Tokyo, Department of Astronomy, Tokyo 113-0033, Japan
⁷⁸ Osaka Prefecture University, Sakai, Osaka 599-8531, Japan
⁷⁹ The University of Tokyo, Institute for Photon Science and Technology, Tokyo, Japan
⁸⁰ Remeis-Observatory and Erlangen Centre for Astroparticle Physics, FAU Erlangen-Nürnberg, Sternwartstr. 7, 96049 Bamberg, Germany
⁸¹ SLAC National Accelerator Laboratory, Kavli Institute for Particle Astrophysics and Cosmology (KIPAC), Menlo Park, CA 94025, USA
⁸² Kurume University, Kurume, Fukuoka 830-0011, Japan
⁸³ Lawrence Berkeley National Laboratory (LBNL), Physics Division, Berkeley, CA 94720, USA
⁸⁴ Space Science Data Center, Italian Space Agency, via del Politecnico, 00133 Roma, Italy
⁸⁵ Centre National d'Etudes Spatiales (CNES), Paris, France

- ⁸⁶ INAF - Astronomical Observatory of Trieste, Trieste, Italy
- ⁸⁷ INAF, Osservatorio Astronomico di Padova, Vicolo dell' Osservatorio 5, 35122 Padova, Italy
- ⁸⁸ Gran Sasso Science Institute (GSSI), Viale F. Crispi 7, 67100 L'Aquila, Italy
- ⁸⁹ Research Center for Nuclear Physics, Osaka University, Ibaraki, Osaka 567-0047, Japan
- ⁹⁰ Yokohama National University, Yokohama, Kanagawa 240-8501, Japan
- ⁹¹ Konan University, Hyogo, Japan
- ⁹² Institute of Astrophysics, FORTH, Heraklion, Greece
- ⁹³ Physics and Astronomy Department, University College London (UCL), London, UK
- ⁹⁴ Department of Physics & Astronomy, University of British Columbia, 6224 Agricultural Road, Vancouver, BC V6T1Z1, Canada
- ⁹⁵ National Institute of Technology, Kagawa College, Mitoyo, Japan
- ⁹⁶ Three-Speed Logic, Inc., Houston, USA
- ⁹⁷ CNRS-UCB International Research Laboratory, Centre Pierre Bintruy, UMI2007, Berkeley, CA 94720, USA
- ⁹⁸ Department of Physics, The University of Tokyo, Tokyo 113-0033, Japan
- ⁹⁹ Dipartimento di Fisica, Universit di Pisa, Largo B. Pontecorvo 3, 56127 Pisa, Italy
- ¹⁰⁰ Mullard Space Science Laboratory, University College London, London, UK
- ¹⁰¹ San Diego Supercomputer Center, University of California, San Diego, La Jolla, CA, USA